VAMP721 Conformations Unmask an Extended Motif for K^+ Channel Binding and Gating Control[1][CC-BY]

Ben Zhang, Rucha Karnik, Sakharam Waghmare, Naomi Donald, and Michael R. Blatt*

Laboratory of Plant Physiology and Biophysics, University of Glasgow, Glasgow G12 8QQ, United Kingdom

ORCID IDs: 0000-0003-4473-9184 (B.Z.); 0000-0001-6876-4099 (R.K.); 0000-0003-1918-0673 (S.W.); 0000-0002-1873-4286 (N.D.); 0000-0003-1361-4645 (M.R.B.).

Soluble *N*-ethylmaleimide-sensitive factor attachment protein receptor (SNARE) proteins play a major role in membrane fusion and contribute to cell expansion, signaling, and polar growth in plants. The SNARE SYP121 of *Arabidopsis thaliana* that facilitates vesicle fusion at the plasma membrane also binds with, and regulates, K^+ channels already present at the plasma membrane to affect K^+ uptake and K^+-dependent growth. Here, we report that its cognate partner VAMP721, which assembles with SYP121 to drive membrane fusion, binds to the KAT1 K^+ channel via two sites on the protein, only one of which contributes to channel-gating control. Binding to the VAMP721 SNARE domain suppressed channel gating. By contrast, interaction with the amino-terminal longin domain conferred specificity on VAMP721 binding without influencing gating. Channel binding was defined by a linear motif within the longin domain. The SNARE domain is thought to wrap around this structure when not assembled with SYP121 in the SNARE complex. Fluorescence lifetime analysis showed that mutations within this motif, which suppressed channel binding and its effects on gating, also altered the conformational displacement between the VAMP721 SNARE and longin domains. The presence of these two channel-binding sites on VAMP721, one also required for SNARE complex assembly, implies a well-defined sequence of events coordinating K^+ uptake and the final stages of vesicle traffic. It suggests that binding begins with VAMP721, and subsequently with SYP121, thereby coordinating K^+ channel gating during SNARE assembly and vesicle fusion. Thus, our findings also are consistent with the idea that the K^+ channels are nucleation points for SNARE complex assembly.

Soluble *N*-ethylmaleimide-sensitive factor attachment protein receptor (SNARE) proteins play a major role in membrane fusion for the targeting and delivery of membrane, protein, and soluble cargo. They contribute to neurotransmitter release in animals, to budding and growth in yeast, and to cell expansion, signaling, and polar growth in plants (Jahn and Scheller, 2006; Lipka et al., 2007; Bassham and Blatt, 2008). Cognate SNAREs localize to vesicle and target membranes, assembling in complex to overcome the large dehydration forces associated with bringing two lipid bilayers together to drive membrane fusion. In vivo, SNARE assembly also serves to ensure the correct targeting of vesicles to their destinations.

SNAREs are classified as Q (Gln)- and R (Arg)-SNAREs according to the amino acid residue each SNARE protein contributes to the central layer formed between the four cognate peptides in complex (Fasshauer et al., 1998; Bock et al., 2001; Grefen and Blatt, 2008). Normally, a SNARE complex assembles with three Q-SNAREs (Qa, Qb, and Qc) and one R-SNARE. R-SNAREs usually are localized to the vesicle membrane and often are referred to as vesicle-associated membrane proteins, or VAMPs. VAMPs can be subdivided into two groups: short VAMPs, or brevins, and long VAMPs, or longins (Rossi et al., 2004). To date, plant genomes have been found to encode only longins (Bassham and Blatt, 2008), each consisting of a single C-terminal transmembrane domain, a central R-SNARE motif, and an N-terminal longin domain (Filippini et al., 2001). The three-dimensional structures of longin domains from several R-SNAREs have been solved (Gonzalez et al., 2001; Tochio et al., 2001). These analyses indicate that the domain forms a paddle-like structure, containing a five-stranded β-sheet core sandwiched between an α-helix on one side and two α-helices on the other. This structure is consistent with its ability to fold and for the SNARE motif to wrap around the longin domain and mask its exposure to the cytosol when not in a SNARE complex (Kent et al., 2012).

[1] This work was supported by the Chinese Scholarship Council (studentship to B.Z.) and by the Biotechnology and Biological Sciences Research Council (grant nos. BB/I024496/1, BB/K015893/1, BB/L001276/1, BB/M01133X/1, BB/M001601/1, and BB/L019205/1 to M.R.B.).

* Address correspondence to michael.blatt@glasgow.ac.uk.

The author responsible for distribution of materials integral to the findings presented in this article in accordance with the policy described in the Instructions for Authors (www.plantphysiol.org) is: Michael R. Blatt (michael.blatt@glasgow.ac.uk).

B.Z. carried out the SUS assays and confocal and oocyte studies with N.D. and M.R.B.; B.Z. and R.K. designed constructs and vectors; R.K., S.W., N.D., and B.Z. carried out immunoblot and biochemical analyses; B.Z., R.K., and M.R.B. wrote the article.

www.plantphysiol.org/cgi/doi/10.1104/pp.16.01549

R-SNAREs of the model plant Arabidopsis (*Arabidopsis thaliana*) show some homologies to VAMP7, an endomembrane R-SNARE found in neuromuscular tissues (Sanderfoot, 2007). Nonetheless, the eight members of the VAMP72 subgroup of proteins are unique to green plants and, with few exceptions, are responsible primarily for secretion at the plasma membrane (Uemura et al., 2004; Sanderfoot, 2007; Zhang et al., 2015). The R-SNAREs VAMP721 and VAMP722 assemble in complex with the plasma membrane Qa-SNARE SYP121 (Karnik et al., 2013b, 2015). SYP121 also binds with the K^+ channels KC1 and KAT1, altering channel gating to promote K^+ uptake and conferring a voltage dependence to secretory traffic for growth (Honsbein et al., 2009, 2011; Grefen et al., 2010, 2015). Binding with SYP121 has been shown to promote vesicle traffic with osmotic solute uptake, including that of K^+, effectively coordinating the two processes and maintaining turgor as the cell expands (Karnik et al., 2017).

Intriguingly, we found that VAMP721 binding suppresses channel activity (Zhang et al., 2015) in a manner opposing that of SYP121, and overexpressing the R-SNARE suppressed K^+-dependent root growth. These and additional observations were consistent with a binding exchange between the R- and Qa-SNAREs coordinating SNARE complex assembly with ion transport, but they raised questions about the binding domain on VAMP721 for the K^+ channels, the conformational changes necessary for channel binding, and the sequence of K^+ channel interactions between the two SNARE proteins. Here, we report that binding of the K^+ channels with the VAMP721 longin domain is associated with a linear sequence of amino acid residues centered on Tyr-57 and necessary for channel binding to the full-length R-SNARE. We also report that a second site, associated with the SNARE domain, is critical for channel gating control. Access to this second site depends on the conformation of the longin domain and its coordination with the SNARE domain, and this process also is associated with the residues around Tyr-57. These findings lead to the proposal that the longin domain of VAMP721 forms a closed structure with Tyr-57 at its center, and this structure aids in positioning VAMP721 to facilitate K^+ channel interaction as well as in initiating its coordination with the cognate SNARE proteins.

RESULTS

VAMP721 Harbors K^+ Channel-Binding Sites in the Longin and SNARE Domains

Our previous studies indicated that VAMP721, but not the endomembrane VAMP723, interacts with the KAT1 and KC1 K^+ channels through a binding site associated with the residue Tyr-57 in the longin domain of the R-SNARE (Zhang et al., 2015). These studies offered no further details of the binding domain(s) or whether binding might be associated with the SNARE domain, as has been reported in animals (Lvov et al., 2008; Tsuk et al., 2008). To resolve the extent of the binding site, we prepared truncated proteins of VAMP721 and VAMP723 and investigated their interaction with the KAT1 K^+ channel using the yeast mating-based split-ubiquitin system (mbSUS) assay, as described before (Grefen et al., 2007; Zhang et al., 2015). VAMP721 and VAMP723 were divided into three regions (Fig. 1A; Supplemental Fig. S1) comprising the longin domain, the SNARE domain, and the transmembrane domain, with two breaks at the junctions Asp-126Glu-127 and Arg-185Lys-186 for VAMP721 and Asp-126Glu-127 and Arg-181Lys-182 for VAMP723.

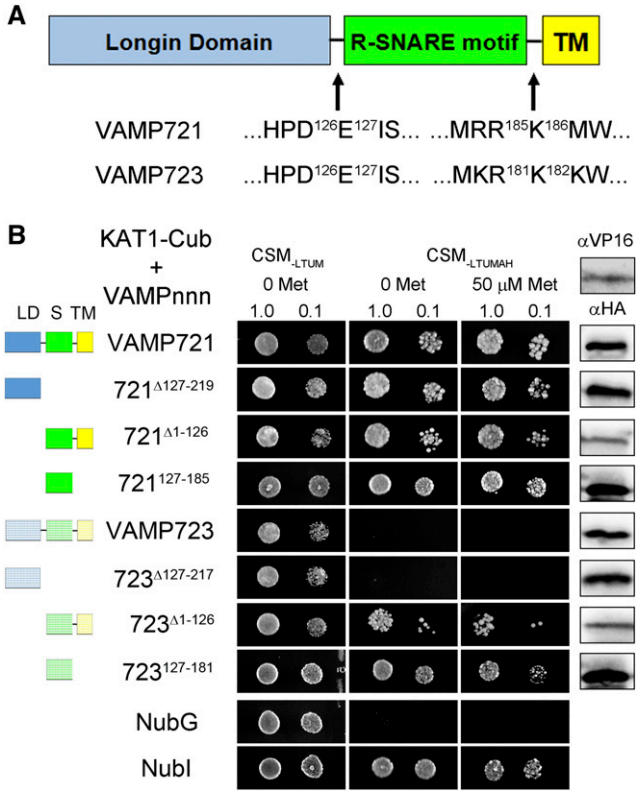

Figure 1. The longin and SNARE domains of VAMP721 interact with the KAT1 K^+ channel. A, The longin domain (blue), the SNARE domain (R-SNARE motif; green), and the transmembrane domain (TM; yellow) are shown with sequence breaks used in the protein expression of VAMP721 and VAMP723 as shown. B, Diploid yeast expressing KAT1-Cub as bait with NubG-X fusions of different truncated VAMPs and controls (negative, NubG; positive, NubI) as prey were spotted onto different media as indicated. VAMP721 and VAMP723 were included for comparison. Cartoons (left) provide a guide to the expressed domains. Data are from one of three independent experiments. Growth on CSM_{LTUM} was used to verify the presence of both bait and prey expression. CSM_{LTUMAH} was used to verify adenine- and His-independent growth of the yeast diploids. The addition of 50 μM Met to CSM_{LTUMAH} was used to verify interaction with KAT1-Cub expression suppressed. Yeast were dropped at 1 and 0.1 optical density at 600 nm (OD_{600}) in each case. Incubation time was 24 h for the CSM_{LTUM} plate and 72 h for CSM_{LTUMAH} plates. Western-blot analysis (5 μg of total protein per lane) of the haploid yeast used in mating (right) used αHA antibody for the VAMP fusions and αVP16 antibody for the K^+ channel fusions.

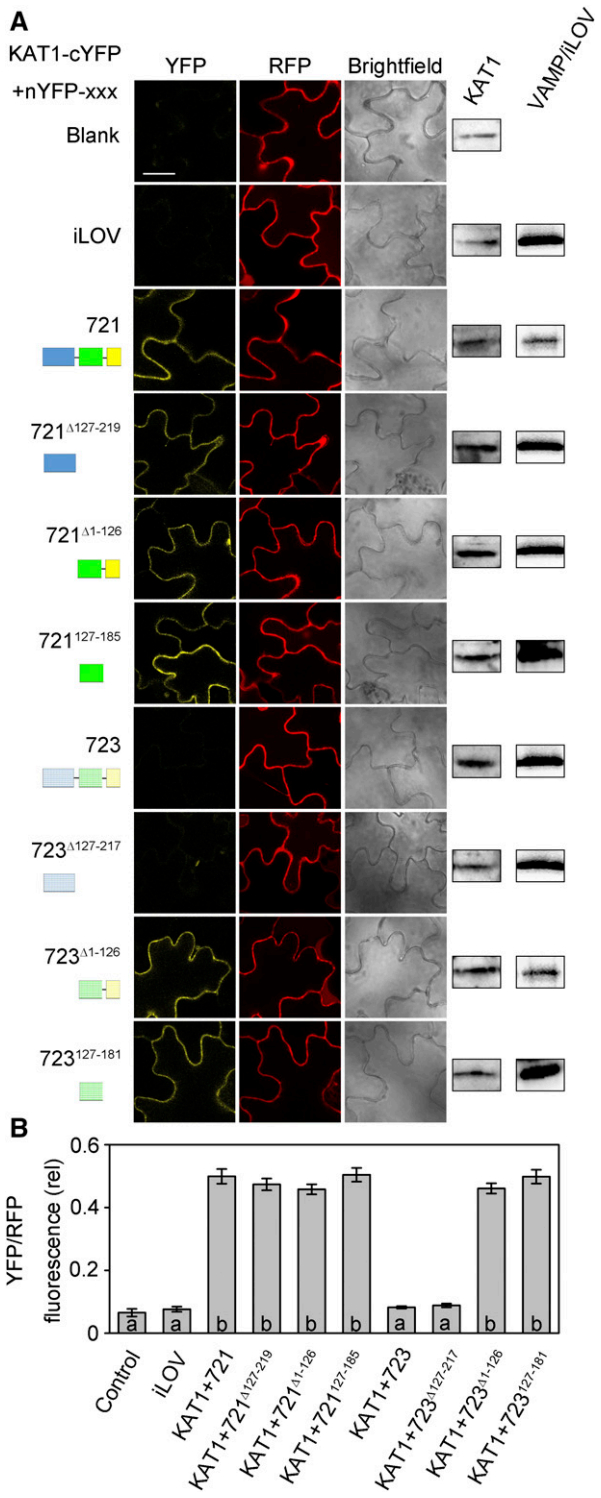

Figure 2. The longin and SNARE domains of VAMP721 interact with the KAT1 K^+ channel in vivo. rBiFC analysis shows KAT1 interaction with VAMP721 and VAMP723 and with their truncations. Yellow fluorescent protein (YFP) and red fluorescent protein (RFP) fluorescence was collected from tobacco transformed using the pBiFCt-2in1-NC (Grefen and Blatt, 2012) 2in1 vector. A, Images are (left to right) YFP (rBiFC) fluorescence, RFP fluorescence, and bright field. Constructs (top to bottom) expressed KAT1-cYFP with the empty cassette (Control) or nYFP-X fusions with iLOV as a negative control and with VAMP721, VAMP723, and their truncations. Cartoons (left) provide a guide to the expressed domains. Immunoblot analysis used αHA and αmyc antibodies to verify fusion protein expression (right). Bar = 10 μm. B, rBiFC fluorescence signals from three independent experiments. Each bar represents the mean ± SE of fluorescence intensity ratios of 10 images per experiment taken at random over the leaf surface. rBiFC signals were calculated as the mean fluorescence intensity ratio determined from each image set after subtracting the background fluorescence determined from an equivalent number of images taken from nontransformed tissues. Significance is indicated by letters at $P < 0.01$.

Figure 1B shows the assays from one of three independent experiments, each yielding similar results. For VAMP721, the diploid yeast grew well on the interaction-selective medium CSM_{LTUMAH} when carrying the K^+ channel-Cub fusions with Nub fusions including both the longin domain ($721^{\Delta 127\text{-}219}$) and the SNARE domain ($721^{\Delta 1\text{-}126}$ or $721^{127\text{-}185}$). The longin domain incorporates the Tyr-57 site, so growth with Nub fusions lacking this domain indicated a second binding site associated with the SNARE motif of VAMP721. We carried out parallel assays using VAMP723, which normally does not interact with the K^+ channels (Zhang et al., 2015). Assays with the equivalent protein truncations showed no yeast growth with the Nub fusion of the VAMP723 longin domain ($723^{\Delta 127\text{-}217}$), but growth was recovered with truncated proteins incorporating the VAMP723 SNARE domain ($723^{\Delta 1\text{-}126}$ and $723^{127\text{-}181}$). These results indicated that both the longin and SNARE domains of VAMP721 interact with the K^+ channel; they also suggested that the interaction between a SNARE motif and the K^+ channel is likely to be common among the VAMP72 proteins, at least in this heterologous system.

We assessed the VAMP-KAT1 interactions in vivo, cloning each of the full-length and truncated VAMP fragments into the ratiometric bimolecular fluorescence complementation (rBiFC) 2in1 vector system and transiently transforming tobacco (*Nicotiana tabacum*) leaves as described before (Zhang et al., 2015). Figure 2 shows a set of representative rBiFC fluorescence images from one experiment along with a summary of the results from all three independent experiments. The measurements from tissues expressing the vector with KAT1 alone and with the iLOV protein as the nYFP fusion (Karnik et al., 2013b, 2015) were included as negative controls. iLOV is an unrelated, soluble protein that is expressed constitutively in Arabidopsis (Chapman et al., 2008) and, therefore, is suitable to control for nonspecific interactions of an nYFP fusion construct. All of the constructs made use of coexpression with soluble RFP, which provided a transformation control and allowed ratiometric quantification of the rBiFC fluorescence (Grefen and Blatt, 2012). These results demonstrated a highly significant rBiFC signal when KAT1 was coexpressed with VAMP721 and each of the VAMP721 fragments, but not with VAMP723 or its longin domain ($723^{\Delta 127\text{-}217}$). Thus, in vivo as in the yeast assay, the association of the K^+ channel with the SNARE

domain appeared promiscuous, whereas interaction with the longin domain was specific for VAMP721.

The SNARE Motif, Not the Longin Domain, of VAMP721 Affects K^+ Channel Activity

To explore the functional consequences of different interaction sites of VAMP721 on K^+ channel activity, full-length VAMP721 and VAMP723, and the truncated VAMP fragments, were heterologously expressed with KAT1 in *Xenopus laevis* oocytes to record the K^+ current under voltage clamp (Grefen et al., 2010; Lefoulon et al., 2014; Zhang et al., 2015). Because VAMP721 affects KAT1 current in a stoichiometric fashion (Zhang et al., 2015), we included complementary RNAs (cRNAs) for each of the VAMP constructs in a 1:4 KAT1:VAMP ratio, and expression was verified by immunoblot in each case.

Figure 3 presents the mean, steady-state current-voltage relations from each of seven experiments for KAT1 and each of the combinations along with representative current traces cross-referenced by symbol and representative immunoblots from one experiment. Under voltage clamp, oocytes expressing the VAMP constructs alone and oocytes injected with water showed only background current. Oocytes injected with KAT1 cRNA showed the typical inward-rectifying

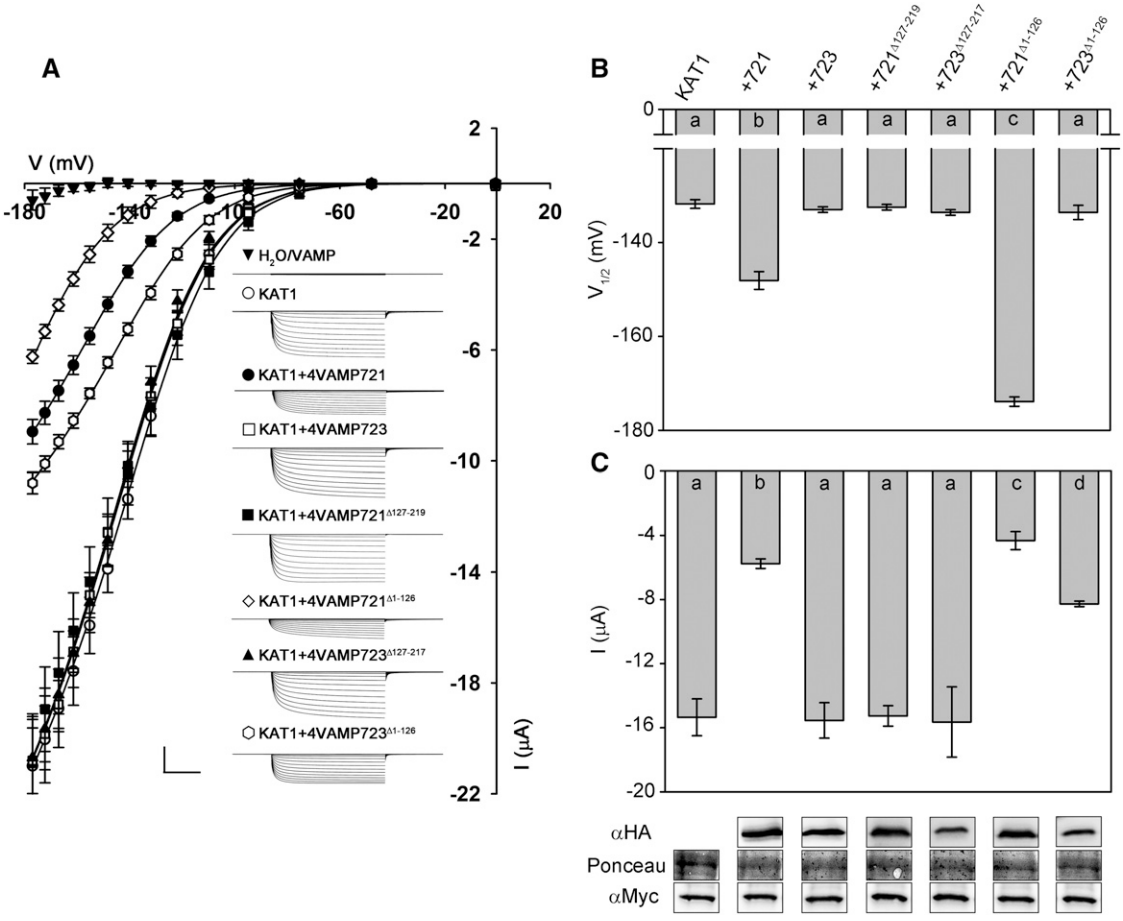

Figure 3. Coexpressing the SNARE, but not the longin domain, of VAMP721 suppresses KAT1 K^+ current. A, Mean steady-state current-voltage curves recorded under voltage clamp in 30 mM K^+ for each set of constructs with oocytes expressing water, VAMP721, and VAMP723 alone (black inverted triangles) and KAT1 alone (white circles) and with VAMP721 (black circles), VAMP723 (white squares), VAMP721$^{\Delta 127\text{-}219}$ (black squares), VAMP721$^{\Delta 1\text{-}126}$ (white diamonds), VAMP723$^{\Delta 127\text{-}217}$ (black triangles), and VAMP723$^{\Delta 1\text{-}126}$ (white hexagons). Data are means ± SE of seven experiments. KAT1 and VAMP cRNAs were coinjected in a 1:4 ratio. Clamp cycles are as follows: holding voltage, −50 mV; voltage steps, 0 to −180 mV; and tail voltage, −50 mV. Representative current traces from one experiment are shown (insets). Solid curves are the results of joint, nonlinear least-squares fitting of the K^+ currents (I_K) to the Boltzmann function (Eq. 1). Best and visually satisfactory fittings were obtained allowing $V_{1/2}$ and g_{max} to vary between curves while holding the voltage-sensitivity coefficient (δ) in common between curves. Scale bars = 10 μA (vertical) and 2 s (horizontal). B and C, Means ± SE for the K^+ channel-gating parameters $V_{1/2}$ (B) and current amplitude at −160 mV (C) recorded from oocytes for the data shown in A. Parameters were derived from joint fittings to a Boltzmann function (Eq. 1). Significance is indicated by letters at $P < 0.01$. Immunoblots verifying VAMP (αHA antibody) and KAT1 (αmyc antibody) expression in oocytes collected after electrical recordings are shown below for one experiment with Ponceau S stain included as a loading control.

K^+ current (Lefoulon et al., 2014). Coexpression with VAMP723 had no visible effect on this current, but coexpression with VAMP721 suppressed the K^+ current, much as reported before (Zhang et al., 2015). Coexpression with the longin domains of the two R-SNAREs, $VAMP721^{\Delta 127\text{-}219}$ and $VAMP723^{\Delta 127\text{-}217}$, also showed no visible effect on the K^+ current. However, coexpression of the $VAMP721^{\Delta 1\text{-}126}$ and $VAMP723^{\Delta 1\text{-}126}$ fragments, incorporating the respective SNARE domains, suppressed the K^+ current in a manner qualitatively similar to that of the full-length VAMP721.

To quantify the characteristics of KAT1 gating, the mean, steady-state current-voltage curves were fitted jointly to a Boltzmann function as

$$I_K = g_{max}(V\text{-}E_K) \Big/ \left(1 + e^{\delta F(V\text{-}V_{1/2})/RT}\right) \quad (1)$$

where g_{max} is the conductance maximum, E_K is the equilibrium voltage for K^+, $V_{1/2}$ is the voltage yielding half-maximal conductance, δ is the apparent gating charge or voltage sensitivity coefficient (Dreyer and Blatt, 2009), V is the membrane voltage, and F, R, and T have their usual meanings. Statistically and visually satisfactory fittings (Fig. 3, solid lines) were obtained with δ held in common and only g_{max} and $V_{1/2}$ allowed to vary between data sets, and these results are included in Table I. KAT1 expression alone yielded a $V_{1/2}$ of −132 mV and a g_{max} of 1.52 mS, much as reported before (Hoshi, 1995; Lefoulon et al., 2014). Coexpressing KAT1 with VAMP723, $VAMP721^{\Delta 127\text{-}219}$, and $VAMP723^{\Delta 127\text{-}217}$ was without effect, but coexpression with VAMP721 and $VAMP721^{\Delta 1\text{-}126}$ reduced g_{max} and displaced $V_{1/2}$ to more negative voltages. With $VAMP723^{\Delta 1\text{-}126}$, the analysis also indicated a decrease in g_{max} and displacement of $V_{1/2}$. Thus, although the longin domain of VAMP721 itself interacts with the KAT1 K^+ channel (Figs. 1 and 2), functional analysis indicated that VAMP721 action on K^+ gating depends on interactions with the R-SNARE motif. The stronger action of the VAMP721 SNARE domain compared with the full-length protein also suggested a role for the longin domain in moderating SNARE motif binding, as if the longin domain affected its interaction with the channels, thus raising questions about the associated interaction surface of the longin domain and its relationship with the SNARE domain.

The VAMP721 Tyr-57 Forms the Core of an Extended K^+ Channel Interaction Motif

Previously, we found that exchange between VAMP721 and VAMP723 of the single residue at position 57 was sufficient to prevent the channel binding of VAMP721 and introduce binding with VAMP723; thus, the $VAMP721^{Y57D}$ mutant failed to interact in mbSUS assays and to alter channel current in oocytes, whereas $VAMP723^{D57Y}$ conferred R-SNARE interaction and gating alterations with the K^+ channel. Other substitutions at this site were less effective. Notably, the $VAMP721^{Y57A}$ substitution showed only marginal effects in its association with KAT1 in yeast (Zhang et al., 2015). Therefore, we used this weakened $VAMP721^{Y57A}$ mutant to test the effects of second, single-site mutants introduced sequentially in an Ala-scanning approach for mbSUS analysis. Figure 4 summarizes the results from one of three independent trials, each yielding similar results, with KAT1 as the bait and with Ala substitutions introduced at residues from Glu-51 to Val-68. These experiments showed strong suppression of yeast growth with Ala substitutions at each residue from Gly-52 to Asn-56 and at residues Leu-58, Val-59, Glu-60, Gly-62, and Tyr-65. These results indicate that an extended, linear sequence of residues, $GHTFNY^{57}LVExGxxY$, is important for the interaction of the VAMP721 longin domain with the K^+ channel.

As a test of the functional consequences of this extended linear sequence in VAMP721, we chose the

Table I. *Coexpressing the SNARE motif of VAMP721 and VAMP723, but not the longin domain, suppresses KAT1 K^+ current and alters channel gating in Xenopus oocytes*

Parameter values are results of joint, nonlinear least-squares fitting of K^+ currents in Figure 3. The cRNAs of KAT1 and VAMPs were coinjected in a 1:4 ratio in all oocytes. Fittings were carried out with the gating charge (δ) held in common, and values for $V_{1/2}$ and g_{max} were allowed to vary between data sets. Data for KAT1 alone, KAT1 + 4VAMP723, KAT1 + $4VAMP721^{\Delta 127\text{-}219}$, and KAT1 + $4VAMP723^{\Delta 127\text{-}217}$ were visually indistinguishable; therefore, g_{max} values were fitted jointly to simplify analysis. Similarly, g_{max} values for KAT1 + 4VAMP721, KAT1 + $4VAMP721^{\Delta 1\text{-}126}$, and KAT1 + $4VAMP723^{\Delta 1\text{-}126}$ were fitted jointly. Data are from seven or more separate experiments for each construct combination and are given as means ± SE. Significance, as the difference from KAT1 expressed alone at $P < 0.01$, is indicated by asterisks.

Sample	$V_{1/2}$	g_{max}	δ
	mV	*S m*$^{-2}$	
KAT1	−131.8 ± 0.9	1.52 ± 0.01	−1.44 ± 0.03
KAT1 + 4VAMP723	−133.0 ± 0.6		
KAT1 + $4VAMP721^{\Delta 127\text{-}219}$	−132.5 ± 0.6		
KAT1 + $4VAMP723^{\Delta 127\text{-}217}$	−133.6 ± 0.6		
KAT1 + 4VAMP721	−148.1 ± 1.9*	0.73 ± 0.02	
KAT1 + $4VAMP721^{\Delta 1\text{-}126}$	−173.9 ± 1.0*	0.80 ± 0.01	
KAT1 + $4VAMP723^{\Delta 1\text{-}126}$	−133.6 ± 1.5		

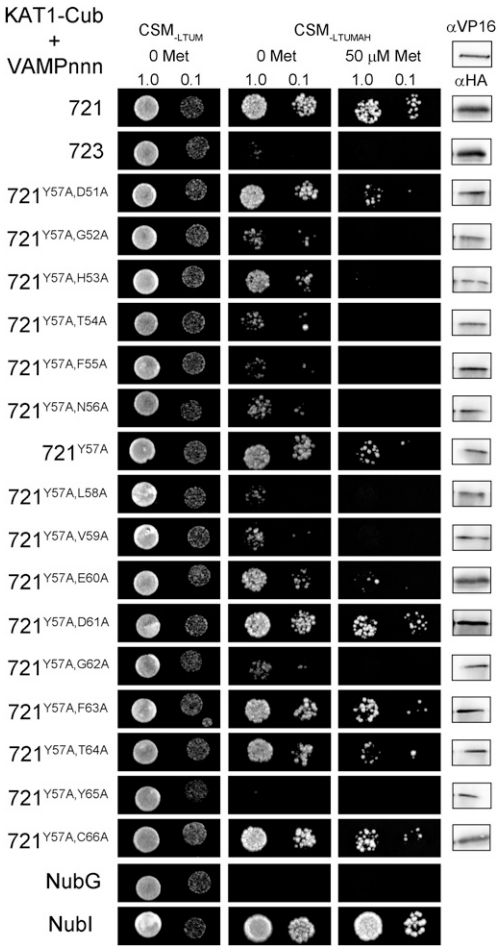

Figure 4. KAT1 interaction with mutants in the VAMP721^{Y57A} background defines the interaction motif GHTFNY^{57}LVExGxxY. Diploid yeast expressing KAT1-Cub as bait with NubG-X fusions of VAMP721^{Y57A} and its double mutants and controls (negative, NubG; positive, NubI) as prey were spotted onto different media as indicated. VAMP721 and VAMP723 were included for comparison. Data are from one of three independent experiments. Growth on CSM_{LTUM} was used to verify the presence of both bait and prey expression. CSM_{LTUMAH} was used to verify adenine- and His-independent growth of the yeast diploids. The addition of 50 μM Met to CSM_{LTUMAH} was used to verify interaction with KAT1-Cub expression suppressed. Yeast were dropped at 1 and 0.1 OD_{600} in each case. Incubation time was 24 h for the CSM_{LTUM} plate and 72 h for CSM_{LTUMAH} plates. Western-blot analysis (5 μg of total protein per lane) of the haploid yeast used in mating (right) used αHA antibody for the VAMP fusions and αVP16 antibody for the K^+ channel fusions.

double mutants VAMP721^{Y57A,F55A}, VAMP721^{Y57A,Y65A}, and, as a control, VAMP721^{Y57A,D61A}. Constructs were prepared for heterologous expression with KAT1 in Xenopus oocytes, in each case in a 1:4 KAT1:VAMP ratio. Again, we recorded the K^+ current under voltage clamp and analyzed the results to extract channel-gating parameters as described above. Figure 5 shows the K^+ current curve for each set along with current traces recorded under voltage clamp from seven or more independent experiments, and it includes a comparative analysis for all of the data along with supporting immunoblot analysis to validate expression. Best fittings of the steady-state currents to Equation 1 were obtained with δ held in common at 1.43 ± 0.04 while allowing g_{max} and $V_{1/2}$ to vary between data sets (Fig. 5; Table II). When coexpressed with KAT1, we found that the wild-type VAMP721 and the interacting mutant VAMP721^{Y57D,D61A} each yielded K^+ currents with similar characteristics, including reduced current amplitudes and a negative shift in $V_{1/2}$. By contrast, coexpressing KAT1 with VAMP721^{Y57D}, VAMP721^{Y57D,F55A}, and VAMP721^{Y57D,Y65A} generated K^+ currents and characteristics that were statistically indistinguishable from those obtained on expressing KAT1 alone. These results indicated that the noninteracting double mutants of VAMP721 prevent R-SNARE-dependent alterations in K^+ channel gating much as does VAMP721^{Y57D}.

Tyr-57 and Residues around It Determine VAMP721 Folding Conformation

Analysis of several R-SNAREs indicates that R-SNARE longin domains form globular structures (Gonzalez et al., 2001; Tochio et al., 2001) that are capable of folding back on the SNARE domain (Pryor et al., 2008; Kent et al., 2012). Because we suspected that Tyr-57 and the residues around it might affect the longin conformation and its interaction with the SNARE domain, we sought to explore this possibility using Förster resonance energy transfer (FRET). The efficiency of FRET energy transfer is high over molecular dimensions and falls off with the sixth power of distance between donor and acceptor fluorophores, making the FRET fluorescence signal ideal for structural studies of proteins and their complexes in vivo (Deniz et al., 2000; Kang et al., 2012; Greitzer-Antes et al., 2013).

For the purpose of analyzing intraprotein conformation, we constructed the intramolecular FRET destination vector pFRET-NcCg-Dest to incorporate a 35S-driven, Gateway-compatible cassette with the mCherry fluorophore as the acceptor at the N terminus and GFP as the donor at the C terminus. Therefore, fusion constructs generated in this vector were flanked at each end by the respective FRET fluorophores (Fig. 6A). We expressed fusion proteins using the cytosolic VAMP721$^{\Delta C}$ fragment shown previously to interact with the channel (Zhang et al., 2015) and to assemble in complex with its cognate SNAREs in vitro (Karnik et al., 2013b). Additionally, we created fusion constructs with the mutant VAMP721$^{\Delta C,Y57A}$, the noninteracting site mutants VAMP721$^{\Delta C,Y57D}$, VAMP721$^{\Delta C,Y57A,F55A}$, and VAMP721$^{\Delta C,Y57A,Y65A}$, and, as a control, the VAMP721$^{\Delta C,Y57A,D61A}$ mutant. We also generated similar fusions with the cytosolic domain of SYP121 for comparison. Previous studies of SYP121 (Karnik et al., 2013b, 2015) indicated that the Habc domain of SYP121 folds back on the Qa-SNARE motif, much as has been reported for several mammalian Qa-SNAREs (Jahn and Scheller, 2006; Bassham and Blatt, 2008; Südhof and Rothman, 2009), and the open conformation of SYP121

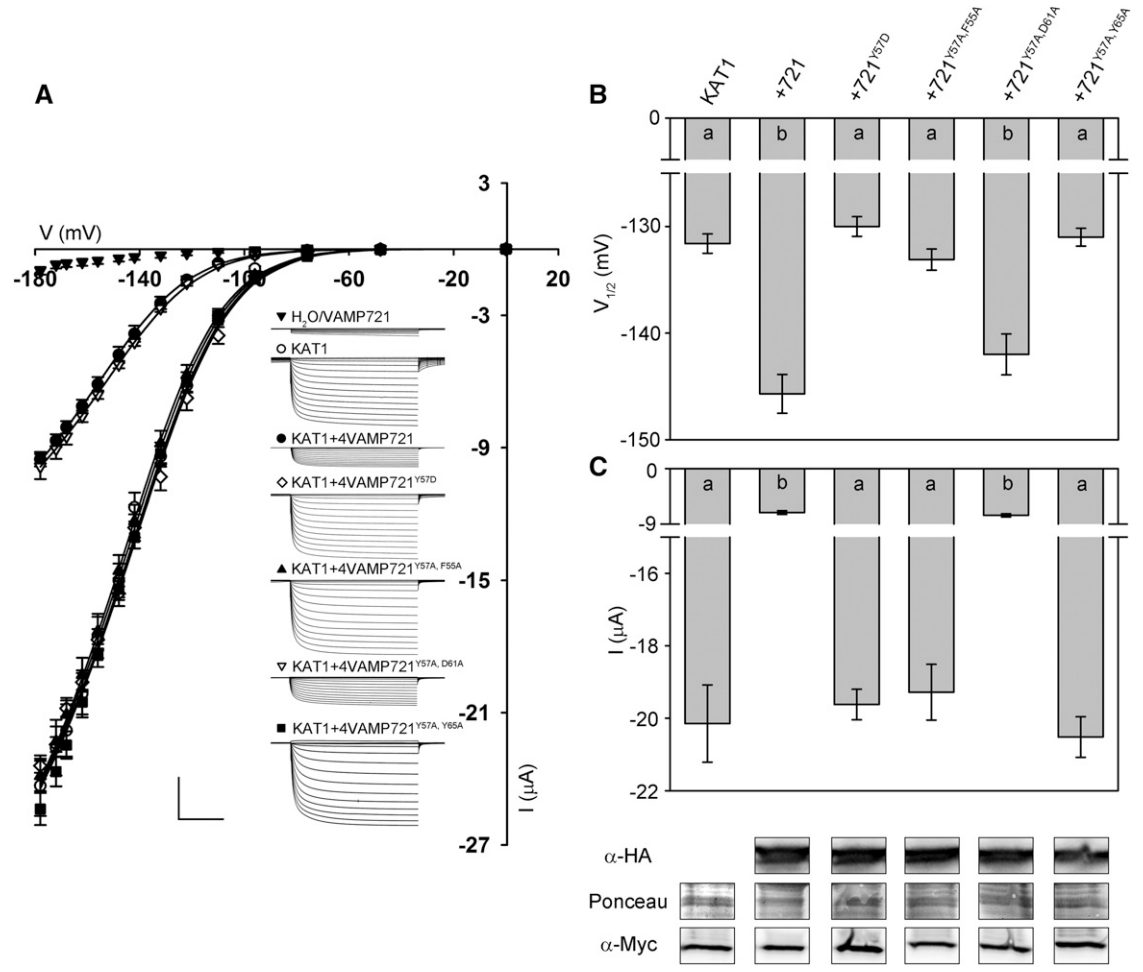

Figure 5. Mutants in the VAMP721^{Y57A} background affecting KAT1 binding also suppress the K^+ current. A, Mean steady-state current-voltage curves recorded under voltage clamp in 30 mM K^+ for each set of constructs with oocytes expressing water and VAMP721 alone (black inverted triangles) and KAT1 alone (white circles) and with VAMP721 (black circles), VAMP721^{Y57D} (white diamonds), VAMP721^{Y57A,F55A} (white triangles), VAMP721^{Y57A,D61A} (white inverted triangles), and VAMP721^{Y57A,Y65A} (black squares). KAT1 and VAMP cRNAs were coinjected in a 1:4 ratio. Clamp cycles were as follows: holding voltage, −50 mV; voltage steps, 0 to −180 mV; and tail voltage, −50 mV. Solid curves are the results of joint, nonlinear least-squares fitting of the K^+ currents (I_K) to a Boltzmann function (Eq. 1). Best and visually satisfactory fittings were obtained allowing $V_{1/2}$ and g_{max} to vary between curves while holding the voltage-sensitivity coefficient (δ) in common between curves. Scale bars = 5 μA (vertical) and 2 s (horizontal). B and C, Means ± SE for the K^+ channel-gating parameters $V_{1/2}$ (B) and current amplitude at −160 mV (C) recorded from oocytes for the data shown in A. Parameters were derived from joint fittings to a Boltzmann function (Eq. 1). Significance is indicated by letters at $P < 0.01$. Immunoblots verifying VAMP (αHA antibody) and KAT1 (αmyc antibody) expression in oocytes collected after electrical recordings are shown below for one experiment with Ponceau S stain included as a loading control.

is stabilized by Ala substitutions of Leu-185 and Glu-186 (Karnik et al., 2013b). Therefore, these fusion constructs of SYP121$^{\Delta C}$ and SYP121$^{\Delta C,L185A,D186A}$ served as positive controls for analysis.

Figure 6B shows representative FRET images from one experiment for each of the constructs, and Figure 6C summarizes the data from three independent experiments. As each construct incorporated both fluorophores, we used GFP fluorescence as a measure of transformation and determined the ratio of mCherry fluorescence to that of GFP to estimate FRET by sensitized emission. These measurements were further validated by acceptor photobleaching. Compared with SYP121$^{\Delta C}$, SYP121$^{\Delta C,L185A,D186A}$ yielded a lower FRET-GFP ratio, consistent with an open conformation of SYP121. Of the VAMP721 constructs, the mutants VAMP721$^{\Delta C,Y57A}$ and VAMP721$^{\Delta C,Y57A,D61A}$ each retained a significant FRET signal. However, each of the mutants VAMP721$^{\Delta C,Y57D}$, VAMP721$^{\Delta C,Y57A,F55A}$, and VAMP721$^{\Delta C,Y57A,Y65A}$ showed a substantial reduction in FRET signal. These results thus paralleled the pattern of K^+ channel interactions observed with the corresponding VAMP721 mutants when expressed in yeast and oocytes (Figs. 3–5).

Table II. *Coexpressing VAMP721^{Y57A,D61A}, but not VAMP721^{Y57A,F55A} or VAMP721^{Y57A,Y65A}, suppresses KAT1 K^+ current and alters channel gating in Xenopus oocytes*

Parameter values are results of joint, nonlinear least-squares fitting of K^+ currents in Figure 5. The cRNAs of KAT1 and VAMPs were coinjected in a 1:4 ratio in all oocytes. Fittings were carried out with the gating charge (δ) held in common, and values for $V_{1/2}$ and g_{max} were allowed to vary between data sets. Data for KAT1 alone, KAT1 + VAMP721^{Y57D}, KAT1 + VAMP721^{Y57A,F55A}, and KAT1 + VAMP721^{Y57A,Y65A} were visually indistinguishable; therefore g_{max} values were fitted jointly to simplify analysis. Similarly, g_{max} values for KAT1 + VAMP721 and KAT1 + VAMP721^{Y57A,Y65A} were fitted jointly. Data are from seven or more separate experiments for each construct combination and are given as means ± SE. Significance, as the difference from KAT1 expressed alone at $P < 0.01$, is indicated by asterisks.

Sample	$V_{1/2}$	g_{max}	δ
	mV	*S m^{-2}*	
KAT1	131.6 ± 0.7	1.75 ± 0.02	1.43 ± 0.04
KAT1 + 4VAMP721^{Y57D}	130.0 ± 0.7		
KAT1 + 4VAMP721^{Y57A,F55A}	133.1 ± 0.7		
KAT1 + 4VAMP721^{Y57A,Y65A}	129.0 ± 0.7		
KAT1 + 4VAMP721	145.7 ± 1.8*	0.75 ± 0.02	
KAT1 + 4VAMP721^{Y57A,D61A}	142.0 ± 1.9*		

As a final test of VAMP721 conformation with these several mutants, we used fluorescence lifetime imaging (FLIM) analysis in four independent experiments to quantify the fluorescence decay lifetimes and their spatial distribution within cells. The presence of an acceptor fluorophore in FRET provides an energy sink for the donor, accelerating its decay from the excited to the ground state (Ishikawa-Ankerhold et al., 2012), and this effect on fluorescence decay kinetics offers an independent measure of FRET that is unaffected by the fluorophore concentration.

To validate FLIM outputs, we compared GFP fluorescence decay on expressing SYP121$^{\Delta C}$-GFP alone with that of the FRET constructs mCherry-SYP121$^{\Delta C}$-GFP and mCherry-SYP121$^{\Delta C,L185A,D186A}$-GFP. These measurements were then repeated with the complementary VAMP721 constructs VAMP721$^{\Delta C}$-GFP, mCherry-VAMP721$^{\Delta C}$-GFP, and mCherry-VAMP721$^{\Delta C,Y57D}$-GFP. In each case, fluorescence decay was fitted to sums of exponentials as

$$F_t = A_1 e^{-t/\tau 1} + A_2 e^{-t/\tau 2}{}_{+\ldots+} A_n e^{-t/\tau n} \quad (2)$$

where A_n is the number of photons at time t and τ_n is the corresponding time constant.

In every case, satisfactory fittings were obtained with two exponential components and are summarized in Figure 7A and Table III. A comparison of the time constants for the two sets of constructs shows that the presence of the mCherry acceptor accelerated GFP fluorescence decay with the SYP121$^{\Delta C}$ and VAMP721$^{\Delta C}$ backbones and that, in each case, the primary effect was on the major component of the fluorescence amplitude. Furthermore, introducing the VAMP721$^{\Delta C,Y57D}$ mutation, like the forced-open Qa-SNARE mutant SYP121$^{\Delta C,L185A,D186A}$, led to a recovery in the kinetics of this relaxation close to that of the fusion constructs with GFP alone.

To validate the changes in relaxation kinetics, we carried out photobleaching studies to locally eliminate the acceptor fluorophore and compare the effects on GFP fluorescence in the same samples. Acceptor photobleaching normally leads to an increase in donor fluorescence if the acceptor would otherwise provide an energy sink; therefore, the fluorescent signal increase of the donor can be used to measure the efficiency of FRET. Figure 7B shows the results from one set of photobleaching experiments with VAMP721$^{\Delta C}$-GFP (left) and mCherry-VAMP721$^{\Delta C}$-GFP (right). The fluorescence plots were taken along the transects shown that span the photobleached areas marked by the boxed regions in the image frames. We determined the mean GFP intensities after and before photobleaching for each of the Qa-SNARE and R-SNARE constructs and calculated the FRET efficiency in each sample as

$$E = (D_a\text{-}D_b)/D_a \quad (3)$$

where D_a and D_b are mean GFP intensities after and before photobleaching, respectively. The results (Fig. 7C) show a high FRET efficiency for VAMP721$^{\Delta C}$, a lesser efficiency for SYP121$^{\Delta C}$, and both declined to a common baseline around 5% with VAMP721$^{\Delta C,Y57D}$ and SYP121$^{\Delta C,L185A,D186A}$ mutants.

Finally, we tested whether the mutation of Tyr-57 affected VAMP721 binding with SYP121 and its assembly in the SNARE complex. For this purpose, we used independent strategies of mbSUS and pull-down assays. The mbSUS assays were carried out using SYP121$^{\Delta C}$ fused to a modified integral membrane protein subunit of the yeast oligosaccharyltransferase complex, mOST4, to provide a bait with an N-terminal anchor, and pull-down assays made use of SYP121$^{\Delta C}$ fused to Protein A (SYP121$^{\Delta C}$-2PA) that retains the capacity for SNARE complex assembly with SNAP33 and VAMP$^{\Delta C}$ (Karnik et al., 2013b, 2015). To improve solubility, the pull-down experiments were carried out with the N-terminally truncated SNAP33$^{\Delta 1\text{-}100}$, which retains its cognate SNARE-binding domains (Supplemental Fig. S2). Figure 8 shows the results from

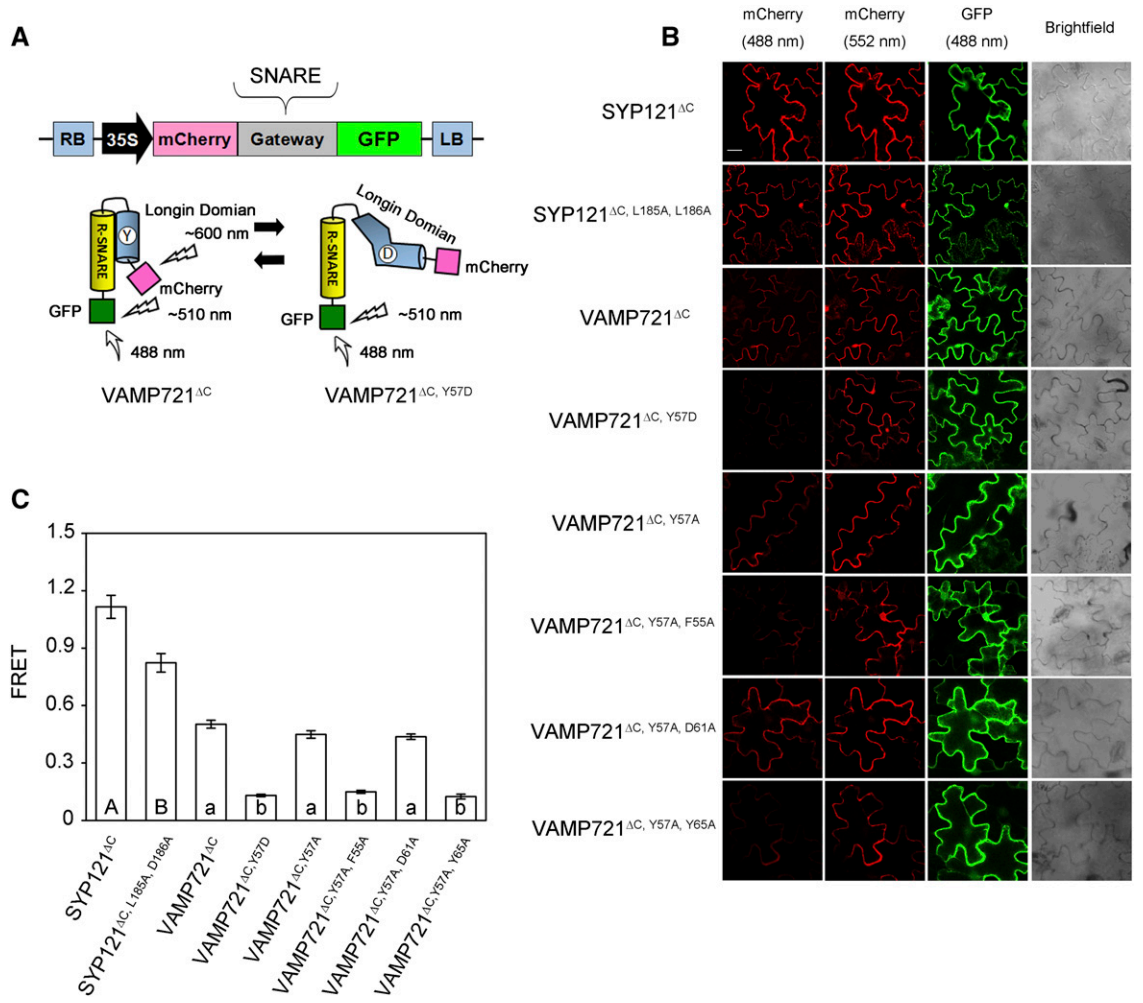

Figure 6. VAMP721 longin domain mutants affecting KAT1 binding are altered in longin-SNARE domain conformation. A, Schematic of the GFP-mCherry FRET pair pFRET-NcCg-DEST vector and conformational interpretations and FRET outputs for the VAMP721$^{\Delta C}$ and VAMP721$^{\Delta C,Y57D}$ constructs. LB, Left border; RB, right border. B, FRET analysis of mCherry and GFP fluorescence by sensitized emission. Images were collected from tobacco transiently transformed with pFRET-NcCg-DEST vector incorporating VAMP721$^{\Delta C}$, VAMP721$^{\Delta C,Y57A}$, VAMP721$^{\Delta C,Y57D}$, VAMP721$^{\Delta C,Y57A,F55A}$, VAMP721$^{\Delta C,Y57A,D61A}$, and VAMP721$^{\Delta C,Y57A,Y65A}$, including SYP121$^{\Delta C}$ and SYP121$^{\Delta C,L185A,D186A}$ as controls. Images are (left to right) mCherry acceptor fluorescence excited with 488-nm light (FRET), mCherry acceptor fluorescence excited with 552-nm light (acceptor reference signal), GFP fluorescence excited with 488-nm light (donor reference signal), and bright field. Bar = 20 μm. C, Mean ± SE of FRET fluorescence ratios from three independent experiments for each of the constructs in B. Data are from each experiment determined from 10 images selected at random over the leaf surface. FRET ratios were calculated as the mean fluorescence intensity ratio [mCherry (488)/mCherry (552)] determined from each image set after subtracting the background fluorescence determined from images taken from nontransformed tissues and validated by acceptor bleaching (see Fig. 10). Data were normalized subsequently to the GFP (488) signal from each image. Significance at $P < 0.01$ is indicated by letters.

one of three experiments in each case, all yielding similar results. Yeast growth was rescued, even in the presence of 500 μM Met, with the mOST4-SYP121$^{\Delta C}$ bait and both the wild-type VAMP721 and the VAMP721^{Y57D} mutant as prey. Similarly, incubating SYP121$^{\Delta C}$-2PA together with SNAP33$^{\Delta 1\text{-}100}$ pulled down the wild-type and mutant R-SNAREs in roughly equal measure. Thus, for VAMP721, the consequence of mutation within the channel-binding motif of the longin domain was to displace the longin domain, notably its N terminus, from that of the C-terminal end of the SNARE domain, but without an appreciable effect on in vitro SNARE complex assembly.

DISCUSSION

Plant growth requires ion transport for osmotic solute uptake and vesicle traffic for membrane and cell wall material delivery. Empirical observations have long shown that these two processes are coordinated to control turgor pressure and cell volume during cell

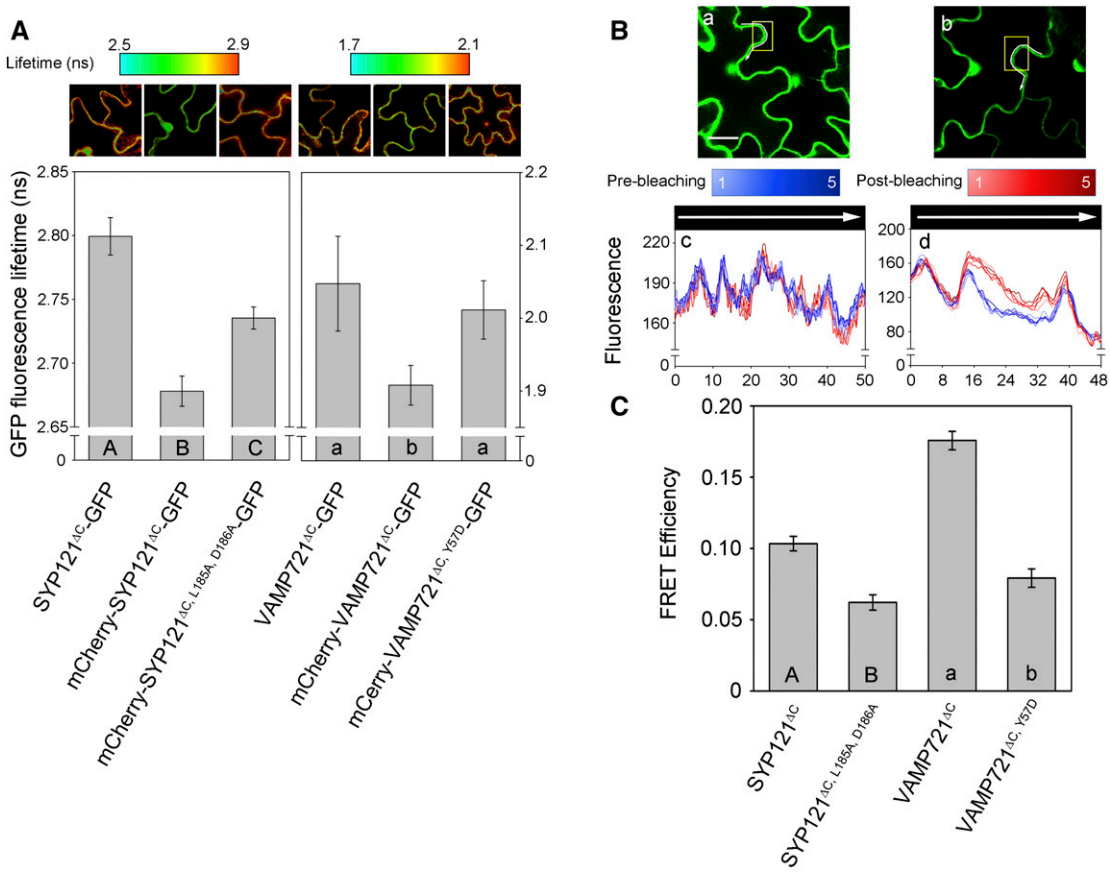

Figure 7. Fluorescence lifetime and photobleaching analyses show that VAMP721$^{\Delta C,Y57D}$ affects the conformational spacing of the longin and SNARE domains. A, FRET fluorescence image analysis of GFP donor fluorescence lifetimes on transiently expressing VAMP721$^{\Delta C}$ and VAMP721$^{\Delta C,Y57D}$ with SYP121$^{\Delta C}$ and SYP121$^{\Delta C,L185A,D186A}$ as controls in the pFRET-NcCg-DEST vector in tobacco. FRET-FLIM data are means ± SE with significance at $P < 0.01$ indicated by letters. Images (above) show pseudocolor-coded GFP fluorescence lifetimes. B, Analysis of GFP fluorescence lifetimes before and after photobleaching with 552-nm light with GFP-VAMP721$^{\Delta C}$ (a) and with GFP-VAMP721$^{\Delta C,Y57D}$-mCherry (b) in the pFRET-NcCg-DEST vector. The photobleach area and line scans taken for analysis are indicated by the yellow squares and the white lines. Five images were recorded each before and after photobleaching. GFP fluorescence before (blue) and after (red) photobleaching along each line scan is shown in c and d. Bar = 20 μm. C, Means ± SE of FRET efficiency from three independent photobleaching experiments calculated as the ratio $(D_a - D_b)/D_a$, where D_a and D_b are the mean GFP intensities after and before photobleaching, respectively. Significance at $P < 0.01$ is indicated by letters.

expansion, but clues to the underlying mechanisms have come to light only recently (Grefen et al., 2011, 2015). Previous reports identified the binding of SYP121, a plasma membrane Qa-SNARE, with KC1 and KAT1 K^+ channels to alter channel gating and channel-mediated K^+ uptake (Honsbein et al., 2009, 2011; Grefen et al., 2010). We now know that SYP121 interacts with the voltage sensor domain of the K^+ channels to confer a voltage dependence on secretory traffic in parallel with K^+ uptake (Grefen et al., 2015). These studies set out the framework for a mutual and concerted mechanism coordinating solute accumulation with the addition of membrane surface area. However, they leave open questions about how SNARE channel binding might integrate within the sequence of events leading to SNARE complex assembly that drives vesicle fusion.

One clue to such integration has come from the discovery that the cognate R-SNARE VAMP721 and its nearly identical homolog VAMP722 interact with the same K^+ channels and that this interaction suppresses channel activity (Zhang et al., 2015). These studies also showed that overexpression of VAMP721 reduces root growth and, similar to the effects of SYP121, that this action is K^+ dependent. It is likely, therefore, that the R-SNARE plays a key role in coordinating vesicle traffic and ion transport in a manner complementary to SYP121. Missing has been information about the conformation(s) of the R-SNARE associated with channel binding, the nature of the binding domains on the R-SNARE, and the sequence of binding events leading to vesicle fusion. We have now built on this previous study, undertaking a detailed analysis of binding with the KAT1 K^+ channel and its implications for VAMP721

Table III. *The value of τ_1 identifies the change of VAMP721 and SYP121 protein conformation*

Parameter values are results of fitting of FLIM in Figure 7A to the sum of two exponential components (Eq. 3). Curve fitting was carried out on histograms of the time-correlated fluorescence signals. Data are given as means ± SE. Significance is indicated by letters at $P < 0.01$.

Sample	τ_1	τ_2
	ns	
Control-SYP121$^{\Delta C}$	2.799 ± 0.015 A	1.341 ± 0.014
SYP121$^{\Delta C}$	2.678 ± 0.011 B	1.342 ± 0.013
SYP121$^{\Delta C,L185A,D186A}$	2.735 ± 0.008 A	1.346 ± 0.014
Control-VAMP721$^{\Delta C}$	1.947 ± 0.065 a	5.823 ± 0.048
VAMP721$^{\Delta C}$	1.808 ± 0.027 b	5.835 ± 0.008
VAMP721$^{\Delta C,Y57D}$	1.911 ± 0.040 a	5.827 ± 0.005

conformation. These studies show that the critical residue Tyr-57 is at the center of a linear sequence predicted to lie within the β-sheet structure of the R-SNARE longin domain and is important for the transition between closed and open conformations of the R-SNARE. The studies also uncover a second domain for K^+ channel binding on VAMP721, associated with the SNARE domain, and indicate that this second site is essential for channel-gating control. On the basis of these discoveries, we suggest that VAMP721 binding with the K^+ channel is likely to occur early in the sequence of conformational transitions leading to vesicle fusion, as it can influence K^+ channel gating only when the R-SNARE motif is not engaged in SNARE complex assembly.

VAMP721 Harbors Two K^+ Channel-Binding Sites

The presence of two domains for interaction with the KAT1 K^+ channel is unequivocal. Both the yeast mbSUS assay for protein-protein interactions and rBiFC analysis in vivo (Figs. 1 and 2) showed that binding is retained with VAMP721 truncations that incorporated either the longin domain or the SNARE domain. Binding with the SNARE domain was unexpected, although interactions of the Kv2.1 K^+ channel in mammals, which depends on the SNARE motif, have been proposed to regulate channel activity during the fusion of dense core vesicles (Lvov et al., 2008; Tsuk et al., 2008). Such interactions with mammalian SNAREs have been questioned in part because, when isolated, the SNARE domains show a high propensity for promiscuous binding in vitro (Fletcher et al., 2003). Indeed, we found that the isolated SNARE domain of VAMP723 also interacted with the KAT1 channel in these assays, even though the full-length VAMP723 does not (Zhang et al., 2015). Although we did not explore the possibility, it is plausible that the transmembrane anchor, too, may associate with the channel protein, if only because, within the membrane bilayer, bait and prey proteins are constrained in their movements to two dimensions (Xing et al., 2016).

What lends credence to our findings with the VAMP721 SNARE domain is its juxtaposition with the VAMP721 longin domain and channel gating. Previously, we reported that VAMP721 binding suppressed KC1 and KAT1 K^+ currents, in each case by reducing the ensemble channel conductance and displacing the voltage sensitivity of the channel to more negative voltages (Zhang et al., 2015). This action was not reproduced by the endomembrane VAMP723 but could be introduced in this R-SNARE by the exchange of Tyr-57 of VAMP721 with Asp-57 of VAMP723. We

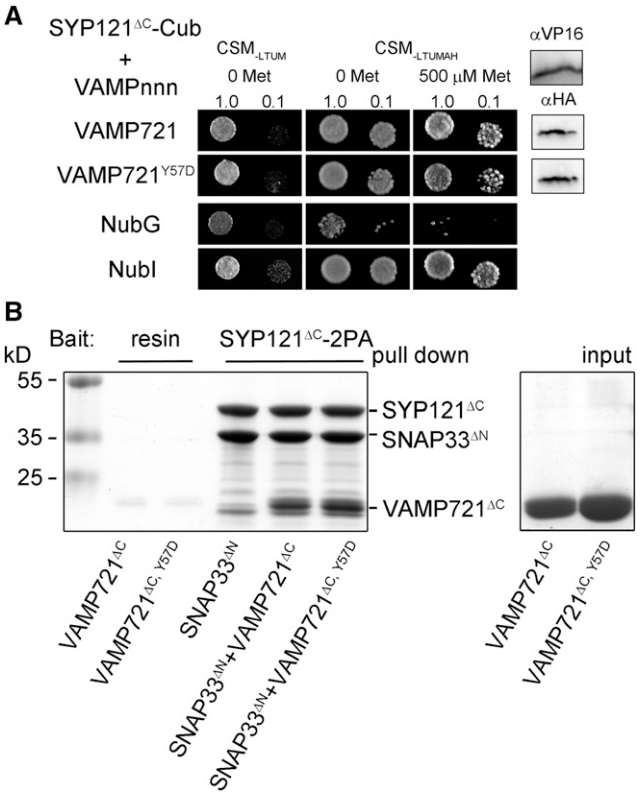

Figure 8. The single-site mutant VAMP721^{Y57D}, which does not interact with the KAT1 channel, is able to bind its cognate SNARE partners and form the SNARE core complex. A, Yeast mbSUS assay using mOST4-SYP121$^{\Delta C}$ as bait and VAMP721 or VAMP721^{Y57D} as prey-alone controls (negative, NubG; positive, NubI). Data are from one of three independent experiments. Growth on CSM$_{LTUM}$ was used to verify the presence of both bait and prey expression. CSM$_{LTUMAH}$ was used to verify adenine- and His-independent growth of the yeast diploids. The addition of 500 μM Met to CSM$_{LTUMAH}$ was used to verify the interaction with suppressed KAT1-Cub expression. Yeast were dropped at 1 and 0.1 OD$_{600}$. Incubation time was 24 h for CSM$_{LTUM}$ and 72 h for CSM$_{LTUMAH}$. Western-blot analysis (5 μg of total protein per lane) of the haploid yeast with αHA antibody (VAMP fusions) and αVP16 antibody (SYP121$^{\Delta C}$) verified the expression of the various constructs (right). B, Coomassie Blue-stained gels showing proteins recovered in pull-down assays using SYP121$^{\Delta C}$-2PA as bait. Lanes are (left to right) the molecular mass marker, VAMP721$^{\Delta C}$ and VAMP721$^{\Delta C,Y57D}$ pull downs with only resin as bait, and pull downs with SNAP33$^{\Delta 1\text{-}100}$ alone, SNAP33$^{\Delta 1\text{-}100}$ + VAMP721$^{\Delta C}$, and SNAP33$^{\Delta 1\text{-}100}$ + VAMP721$^{\Delta C,Y57D}$ using SYP121$^{\Delta C}$-2PA as bait. Equivalent aliquots of the inputs VAMP721$^{\Delta C}$ and VAMP721$^{\Delta C,Y57D}$ are included (right). SYP121$^{\Delta C}$-2PA, SNAP33$^{\Delta 1\text{-}100}$, and VAMP721$^{\Delta C}$ bands are indicated. Proteins were purified, and prey proteins were added in a 5-fold excess to the baits as described previously (Karnik et al., 2013b, 2015).

can show now that these actions are actually associated with the SNARE domain (Fig. 3), even though the longin domain retains binding when isolated in the mbSUS assay and in vivo (Figs. 1 and 2). Qualitatively similar actions were observed with the VAMP721$^{\Delta 1\text{-}126}$ and VAMP723$^{\Delta 1\text{-}126}$ truncations lacking the corresponding longin domains, and an intermediate set of characteristics was observed on coexpressing the full-length VAMP721 with KAT1. In each case, changes in g_{max} might be understood if VAMP coexpression affected the population of channels at the membrane; the displacements in $V_{1/2}$, however, leave no doubt of an action on channel gating (Dreyer and Blatt, 2009; Lefoulon et al., 2014). In short, the functional consequences of VAMP721 binding to the K^+ channel can be ascribed to the VAMP721 SNARE domain, not its longin domain. Thus, although binding with the longin domain of VAMP721 is evident in yeast and in vivo, the two VAMP721 domains appear to act in concert, the SNARE domain influencing channel gating and the longin domain conferring specificity to VAMP721 for binding.

Residues around Tyr-57 of VAMP721 Contribute to K^+ Channel Binding

One explanation for this discovery is that the longin domain functions to regulate access for channel binding to the SNARE domain, possibly through a switch-like mechanism or by facilitating its conformational stability. Regardless of any mechanistic interpretation, these findings imply a more substantial interaction surface for control of the R-SNARE than was recognized previously (Reichmann et al., 2007; Aakre et al., 2015). We used mbSUS assays to explore the contributions of other residues important for KAT1 interaction. Ala substitutions for Gly-52 to Asn-56, Leu-58 to Glu-60, Gly-62, Tyr-65, Val-67, and Val-68 suppressed the association with the K^+ channel (Fig. 4). Most of these residues are conserved in the VAMP72 family (Supplemental Fig. S1). That their contributions were evident only in the VAMP721^{Y57A} background underscores the coordination with the central Tyr-57 in channel binding.

Could Tyr-57 and its surrounding residues affect the VAMP721 conformation and thereby its availability for K^+ channel binding? This central residue aligns closely with Tyr-45 of the neuronal VAMP7/TI-VAMP, which is known to play a crucial role in maintaining a closed conformation with the R-SNARE unavailable for binding in a SNARE core complex (Vivona et al., 2010). The cytosolic polypeptide of VAMP7/TI-VAMP has been crystallized (Pryor et al., 2008; Kent et al., 2012); its structure indicates that the longin domain forms a globular paddle of antiparallel β-strands flanked by α-helices at either side and that the partially unstructured SNARE domain wraps around this paddle (Kent et al., 2012). Mapping VAMP721 to these data (Fig. 9) indicates that the sequence GHTFNY^{57}LVExGxxY is

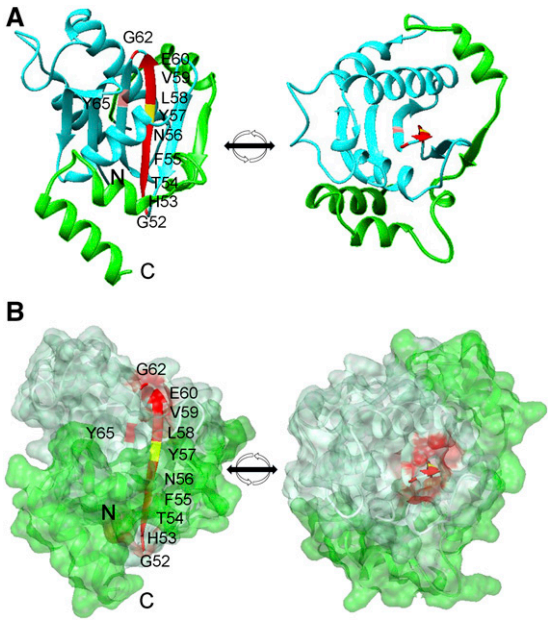

Figure 9. The predicted structure of VAMP721 in ribbon (A) and partially transparent surface (B) representations. Structural predictions were obtained with Phyre2 software (Kelley and Sternberg, 2009) using the structures of the yeast proteins SEC22 and YKT6 as well as VAMP7 from humans (Gonzalez et al., 2001; Tochio et al., 2001; Kent et al., 2012). A, Ribbon structural representation of VAMP721 without the C-terminal transmembrane anchor in side (left) and top (right) views. The top view is rotated 90° about the horizontal axis, with Gly-62 in front. The longin domain is shown in cyan and the SNARE domain in green Residues of the GHTFNY^{57}LVExGxxY motif are indicated by the red β-sheet with the position of Tyr-57 indicated centrally in yellow. B, Transparent space-filling structural representation of VAMP721 as in A in side (left) and top (right) views. The top view is rotated 90° about the horizontal axis, with Gly-62 in front. The longin domain is shown in cyan and the SNARE domain in green Residues of the GHTFNY^{57}LVExGxxY motif are indicated by the red β-sheet with the position of Tyr-57 indicated centrally in yellow.

situated near the base of the longin paddle and forms one half of a hairpin loop around which the SNARE domain is wrapped. It is conceivable, therefore, that mutations affecting the conformation of this hairpin loop are likely to affect access to the SNARE domain, possibly influencing the stability of binding of a cognate partner coordinated between the two sites.

Our analysis of intramolecular FRET supports this idea. These experiments made use of FRET between the two ends of the cytosolic VAMP721$^{\Delta C}$ to explore conformational changes introduced by mutations in the longin hairpin loop. The results showed in VAMP721$^{\Delta C,Y57D}$ a reduced FRET signal compared with that of VAMP721$^{\Delta C}$, consistent with an increased spacing between N and C termini and with substantial, long-distance conformational changes introduced by the mutation. Similar results were obtained with the double mutants VAMP721$^{\Delta C,Y57A,F55A}$ and VAMP721$^{\Delta C,Y57A,Y65A}$ (Fig. 6). Double mutants at each of these sites also failed to interact with KAT1 or to alter its gating (Figs. 4 and

5). By contrast, VAMP721$^{\Delta C,Y57A}$ and the internal control VAMP721$^{\Delta C,Y57A,D61A}$ had no effect on the FRET signal or, in the oocyte assay, a substantial effect on channel interaction and gating (Zhang et al., 2015). Clearly, mutations within the longin hairpin loop, and especially of the central Tyr-57, have substantial effects on VAMP721 conformation, and these effects extend beyond the longin domain to the conformation of the R-SNARE.

A Model for K^+ Channel Binding within the SNARE Cycle

It is puzzling that deletion of the longin domain facilitates binding and alters channel gating by VAMP721$^{\Delta 1\text{-}126}$, even though the same longin domain, and especially the sequence GHTFNY^{57}LVExGxxY, is necessary for binding and the gating alterations mediated by the full-length VAMP721. At present, it is not possible to resolve this seeming paradox unambiguously, but we can offer two general explanations. From the studies presented here, we know that both the longin and SNARE domains bind the K^+ channel, but only the latter affects channel gating. Additionally, gating is more strongly affected by the VAMP721$^{\Delta 1\text{-}126}$ peptide lacking the longin domain than by the full-length VAMP721, and both differ in effect from VAMP723$^{\Delta 1\text{-}126}$ (Fig. 3). Finally, mutation at the core of the GHTFNY^{57}LVExGxxY sequence does not appear to affect SNARE complex assembly (Fig. 8), even though it does alter K^+ channel binding. One explanation, therefore, is that unwrapping the SNARE domain is necessary for channel access and binding to the VAMP721 SNARE domain and that this unwrapping depends on an initial interaction of the channel that is transmitted via the longin hairpin loop. This explanation accounts for the weaker action on gating of the full-length VAMP721, possibly as a consequence of the stochastic process of binding events; it posits that an association with the channel induces a conformational change in VAMP721; and it implies a sequential binding of the channel, first with the longin domain and thereafter with the SNARE domain. The second explanation is that the channel normally binds VAMP721 via both the longin and SNARE domains concurrently and that the unique bilateral coordination gives rise to its specificity. Like the first explanation, this alternative implies that channel association induces conformational changes in VAMP721 leading to their interaction, but it leads to a conclusion that interactions with the VAMP721$^{\Delta 1\text{-}126}$ and VAMP723$^{\Delta 1\text{-}126}$ truncations differ in conformation if not in their effects on channel gating.

Distinguishing between these alternatives will require structural information for the bound complex. Regardless of the conformational details, however, it is clear that channel binding by VAMP721 and by its cognate Qa-SNARE SYP121 dovetails within the sequence of events leading to vesicle fusion. Like VAMP721, SYP121 interacts with both the KC1 and KAT1 K^+ channels, but with opposing effects on channel gating (Honsbein et al., 2009, 2011; Grefen et al., 2010, 2015; Zhang et al., 2015). This functional juxtaposition between the two cognate SNAREs implies a sequential handover in binding with the K^+ channels as the two SNAREs assemble a SNARE complex to drive membrane fusion. We know that SNARE complex assembly requires a tight entwining of the cognate SNARE domains, including those of the Qa- and R-SNAREs. K^+ channel interaction with the VAMP721 SNARE domain is likely to mask it and preclude SNARE complex assembly. However, once unwrapped, channel interaction with the VAMP721 longin domain should free the R-SNARE for binding with SYP121. We also know that channel interaction with

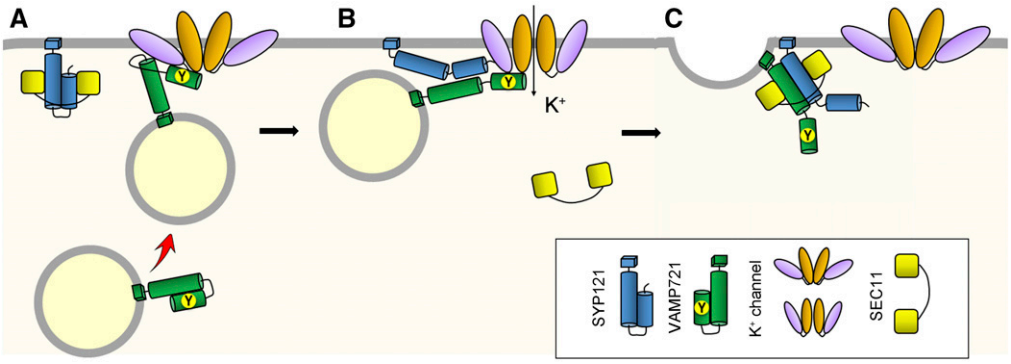

Figure 10. Hypothetical model for K^+ channel exchange between VAMP721 and SYP121 during vesicle fusion. This condensed sequence builds on current knowledge of SNARE complex formation, including the role for the Sec1/Munc18 protein SEC11 (Karnik et al., 2013b, 2015). For clarity, only the SNAREs SYP121 and VAMP721 are shown. A, Vesicle approach with VAMP721 leads to its binding with the K^+ channel through both the longin and SNARE domains, facilitating the unwrapping of the SNARE domain. B, The unwrapped VAMP721-K^+ channel complex recruits SYP121 and unlatches SEC11. Interaction between SYP121 and the K^+ channel, and the release of the VAMP721 SNARE domain, promote channel activity. Not shown for clarity is the relatching of SEC11 to stabilize the SNARE complex for vesicle fusion. C, SNARE complex assembly drives the final stages of membrane fusion followed by release of the channel interaction in preparation for SNARE recycling.

SYP121 associates with the N terminus of the Qa-SNARE, not with its SNARE domain (Grefen et al., 2010), and that this interaction promotes secretory traffic (Grefen et al., 2015).

How might a handover in channel binding be engineered together with SNARE complex assembly? One plausible sequence of events (Fig. 10) is that VAMP721 interaction with the K^+ channel aids in vesicle tethering and helps to unwrap the R-SNARE; the VAMP721-channel complex then recruits SYP121, unlatching the bound Sec1/Munc18 protein SEC11 and unfurling SYP121 (Karnik et al., 2013b, 2015; Grefen et al., 2015); finally, the two SNARE domains coalesce together with the Qb- and Qc-SNARE domains of SNAP33 to drive vesicle fusion (Lipka et al., 2007; Bassham and Blatt, 2008; Karnik et al., 2013b). This sequence implies binding transitions that pass from an interaction that inhibits channel activity (VAMP721 SNARE domain) through one that is activity neutral (VAMP721 longin domain) to one that promotes channel activity (SYP121).

Whether such a sequence proves correct, from the trafficking standpoint what is important is that the evidence posits channel binding as a focal point at which the R- and Qa-SNAREs coalesce, effectively seeding the final stages of SNARE complex assembly and vesicle fusion. Indeed, an estimate of the number of sites needed for vesicle fusion to support cell expansion yields a value that is remarkably close to the number of K^+ channels commonly found at the plant cell plasma membrane (Grefen et al., 2011). These calculations also lead to the conclusion that only a small proportion of the Qa-SNAREs present at the plant plasma membrane are active in vesicle fusion at any one time. Much the same conclusion is reached on considering the processes of vesicle traffic in neuromuscular tissues (Sieber et al., 2007; Murray and Tamm, 2009). In each case, the excess in Qa-SNAREs probably reflects the need to maintain a reservoir of these proteins for secretion and their turnover, and it may be important for their clustering to enhance vesicle sorting to their cognate fusion sites.

In summary, we find that K^+ channel binding to VAMP721 is mediated by two sites distributed over the structure of the R-SNARE. One site is associated with a linear sequence of residues centered around Tyr-57 and located near the base of the paddle-like longin domain. The second site is associated with the SNARE domain and accounts for the alterations in channel gating, K^+ uptake, and plant growth reported previously. Specificity for K^+ channel binding depends on the longin domain, although this domain does not appear to affect channel gating. Finally, mutations of key residues in the linear sequence around Tyr-57 affect the physical spacing between the longin and SNARE domains and alter the capacity for channel binding that affects channel gating. The presence of these two channel-binding sites on VAMP721, one also required for SNARE complex assembly, implies a well-defined sequence of events, beginning with channel binding with VAMP721, to coordinate K^+ channel gating with SNARE assembly, leading to vesicle fusion.

MATERIALS AND METHODS

Molecular Biology

The pFRET-NcCg-Dest vector was prepared by digesting pFRETgc-2in1-Dest (Hecker et al., 2015) using *Sal*I restriction sites situated between the *ccdB* gene and the *att*R2 site. The vector backbone was ligated, and subsequent transformation and selection were in *ccdB*-survival *Escherichia coli* cells (Life Technologies). The resultant plasmid sequence was verified by restriction endonuclease digestion and sequencing (GATC Biotech).

Open reading frames for KAT1 and the full-length or truncated VAMPs were amplified with gene-specific primers that included Gateway attachment sites (*att*B1/*att*B2) as described before (Zhang et al., 2015). Entry clones SYP121$^{\Delta C}$, SYP121$^{\Delta C,L185A,D186A}$, VAMP721^{Y57D}, VAMP721^{Y57A}, and KAT1 were described previously (Karnik et al., 2013b, 2015; Lefoulon et al., 2014; Zhang et al., 2015). Gateway destination clones were generated using LR Clonase II (Life Technologies). Second-site mutants were generated by site-directed mutagenesis (Karnik et al., 2013b) with the entry clone VAMP721^{Y57A} used as the template. Primers for point mutations (Supplemental Table S1) were designed by SDM-Assist software (Karnik et al., 2013a) to include unique silent restriction sites along with the desired mutation for later identification by restriction endonuclease digestion.

For split-ubiquitin system assays, KAT1 was recombined in pMetYC-Dest (Grefen et al., 2009). VAMP constructs were recombined in pNX35-Dest. For electrophysiological analysis, KAT1 was recombined in pGT-Dest, which introduced a C-terminal myc tag, and the VAMP constructs were recombined in pGT-nHA-Dest (Zhang et al., 2015). For FRET analysis, all constructs were introduced into the pFRET-NcCg-Dest vector. Gateway entry clones and destination clones were amplified using Top10 cells (Life Technologies) with the appropriate antibiotic, either 20 mg L^{-1} gentamicin for entry clones or 100 mg L^{-1} spectinomycin for destination clones.

For protein expression and pull-down assays, we used the truncated recombinant SYP121 fused to protein A, SYP121$^{\Delta C}$-2PA, as described previously (Karnik et al., 2013b). Additionally, the pETDuet vector was modified to express the cognate SNARE proteins with C-terminal Flag (DYKDDDDK) or 6× His tags. We truncated SNAP33 to generate SNAP33$^{\Delta 1\text{-}100}$ and improve solubility during purification without affecting the cognate SNARE domains. Flag-tagged VAMP721$^{\Delta C}$ and VAMP721$^{\Delta C,Y57D}$ proteins were constructed as before. For cloning, SNAP33$^{\Delta 1\text{-}100}$ was amplified by PCR to add 5′ *Nco*I and 3′ *Bst*BI sites, and VAMP721$^{\Delta C}$ was amplified to add 5′ *Nco*I and 3′ *Kpn*I sites before ligation into the modified pETDuet vector. VAMP721$^{\Delta C,Y57D}$ was generated by site-directed mutagenesis as described previously (Karnik et al., 2013b). Supplemental Table S1 includes the primers used for cloning the SNAREs in the *E. coli* expression vector, and Supplemental Figure S2 details the SNAP33 truncation.

mbSUS Assays

The haploid yeast strains THY.AP4 and THY.AP5 (Obrdlik et al., 2004) were transformed as described previously (Grefen et al., 2009). Yeast mbSUS assays were performed with pools of 10 to 15 yeast colonies selected and inoculated into selective medium (CSM_{LM} for THY.AP4 and CSM_{MTU} for THY.AP5) for overnight growth at 180 rpm and 28°C. Liquid cultures were harvested and resuspended in yeast peptone dextrose (YPD) medium. Yeast mating was performed in sterile PCR tubes by mixing equal aliquots of cultures containing KAT1-Cub in THY.AP4 with the appropriate NubG-VAMP in THY.AP5. Aliquots of 5 μL were dropped on YPD plates and incubated at 28°C overnight. Colonies were transferred from YPD onto CSM_{LMTU} plates and incubated at 28°C for 2 to 3 d. Diploid colonies were selected and inoculated in liquid CSM_{LMTU} medium and grown at 180 rpm and 28°C overnight before harvesting and resuspension in sterile water. Serial dilutions at OD_{600} of 1 and 0.1 in water were dropped, 5 μL per spot, on CSM_{AHLMTU} plates without and with Met added at increasing concentrations. Plates were incubated at 28°C, and images were taken after 3 d. Yeast also were dropped on CSM_{LMTU} control plates to confirm mating efficiency and cell density, and growth was monitored after 24 h at 28°C. To verify expression, yeast were harvested in aliquots equal to those used for the dilution series and extracted for protein gel-blot analysis using commercial αHA antibody for NubG and commercial αVP16 antibody (Abcam) for the Cub fusions.

Pull-Down Assays

Protein expression was induced in *E. coli* BL21DE3 cells (Life Technologies) with 1 mM isopropyl β-D-1-thiogalactopyranoside for 4 h. Expressed proteins were purified by affinity chromatography using nickel-nitrilotriacetic acid agarose- or IgG-coupled Sepharose resin as described previously (Karnik et al.,

2013b, 2015). SYP121$^{\Delta C}$ was immobilized as bait. Truncated proteins for the Qa-, Qb-, and Qc-SNAREs were used to eliminate hydrophobic residues that reduce SNARE solubility and were generated as before to avoid affecting binding domains essential for the SNARE complex (Karnik et al., 2013b, 2015). Pull downs included controls for the baits on resin alone, and prey proteins were included in 5-fold excess to baits.

Sensitized Emission FRET and FRET-FLIM Analyses

Confocal images were collected using a Leica TCS SP8-SMD confocal microscope with a PicoQuant FLIM system and spectral GaAsP detectors. Images were collected using a 20×/0.75NA objective lens. For FRET studies, GFP fluorescence was excited with continuous 488-nm or 20-MHz pulsed 470-nm light and collected over 500 to 535 nm. mCherry fluorescence was collected over 590 to 645 nm. mCherry also was detected separately with excitation at 552 nm, and the same laser wavelength was used for mCherry photobleaching. Changes in FRET were calculated from the mCherry-GFP fluorescence ratio (Greitzer-Antes et al., 2013). Photobleaching studies typically were carried out with five scans to establish the prebleach baseline before photobleaching with 552-nm light followed by five scans to collect the postbleach data. Fluorescence lifetime data were acquired until sample sizes exceeded 2,000 photons per pixel. Lifetimes were calculated for all pixels within the 256 × 256 pixel frame. Time-correlated single-photon counting histograms containing the accumulated decay signals were used for fitting to sums of exponentials and to determine the decay time constants using SymPhoTime64 software (PicoQuant).

rBiFC Analysis

Confocal images for rBiFC were collected as described above with a 40×/1.30NA oil objective lens. YFP and RFP were excited with 514- and 552-nm light. YFP and RFP fluorescence emissions were collected over 520 to 565 nm and 560 to 615 nm, respectively. rBiFC fluorescence ratios were calculated as described previously after subtracting background fluorescence recorded from nontransformed tissues prepared in parallel (Blatt and Grefen, 2014; Grefen et al., 2015; Zhang et al., 2015).

Electrophysiology

For electrical recordings from *Xenopus laevis* oocytes, plasmids were linearized, and capped cRNA was synthesized in vitro using the T7 mMessage Machine (Ambion). cRNA was verified by gel electrophoresis before mixing to give the desired molar ratios noted. Mixture volumes were adjusted to the standard volume using RNase-free water. Stage VI oocytes were isolated from mature *X. laevis*, and the follicular cell layer was digested with 2 mg mL^{-1} type 1A collagenase (Sigma-Aldrich) for 20 min before injection. Following injections, oocytes were incubated in ND96 buffer (96 mM NaCl, 2 mM KCl, 1 mM $MgCl_2$, 1 mM $CaCl_2$, and 10 mM HEPES-NaOH, pH 7.4) supplemented with gentamicin (5 mg L^{-1}) at 18°C for 3 d before electrophysiological recordings.

Whole-cell currents were recorded under voltage clamp using an Axoclamp 2B two-electrode voltage-clamp circuit (Axon Instruments) as described previously (Leyman et al., 1999; Sutter et al., 2006). Measurements were performed under continuous perfusion with 30 mM KCl and 66 mM NaCl with additions of 1.8 mM $CaCl_2$ and 10 mM HEPES-NaOH, pH 7.2. A standard voltage-clamp cycle was used with a holding voltage of −50 mV and voltage steps from 0 to −180 mV. Oocytes yielding currents were collected, and total membrane protein was isolated (Sottocornola et al., 2006) using 20 μL of extraction buffer per oocyte. Protein expression was verified using commercial antibodies (Abcam) to myc (KAT1) and HA (VAMP) epitopes.

Plant Growth and Transformation

Wild-type tobacco (*Nicotiana tabacum*) plants were grown in soil at 26°C and 70% relative humidity on a 16/8-h day/night cycle for 4 to 6 weeks. Plants with three to four fully expanded leaves were selected and infiltrated with *Agrobacterium tumefaciens* GV3101 carrying the desired constructs as described previously (Tyrrell et al., 2007; Blatt and Grefen, 2014).

Statistics

Statistical analysis of independent experiments is reported as means ± SE as appropriate with significance determined by Student's *t* test or ANOVA. To avoid substantial indetermination, standard methods for joint fittings were applied with one or more selected parameters held in common between data sets (Honsbein et al., 2009; Grefen et al., 2010; Lefoulon et al., 2014; Zhang et al., 2015). All fittings were by nonlinear least-squares minimization using a Marquardt-Levenberg algorithm (Marquardt, 1963) as implemented in SigmaPlot version 11.2 (Systat Software).

Accession Numbers

Sequence data from this article can be found in the GenBank/EMBL data libraries under accession numbers At3g11820 (SYP121), At1g12360 (SEC11), At1g04750 (VAMP721), and At5g01010 (SNAP33).

Supplemental Data

The following supplemental materials are available.

Supplemental Figure S1. Alignment of the longin domain of VAMP amino acid sequences.

Supplemental Figure S2. SNAP33 structure and its truncation.

Supplemental Table S1. Oligonucleotides that were designed to construct the clones used in this study.

ACKNOWLEDGMENTS

We thank Amparo Ruiz-Pardo and George Boswell for support in plant and *X. laevis* maintenance.

Received October 6, 2016; accepted November 4, 2016; published November 7, 2016.

LITERATURE CITED

Aakre CD, Herrou J, Phung TN, Perchuk BS, Crosson S, Laub MT (2015) Evolving new protein-protein interaction specificity through promiscuous intermediates. Cell **163:** 594–606

Bassham DC, Blatt MR (2008) SNAREs: cogs and coordinators in signaling and development. Plant Physiol **147:** 1504–1515

Blatt MR, Grefen C (2014) Applications of fluorescent marker proteins in plant cell biology. Methods Mol Biol **1062:** 487–507

Bock JB, Matern HT, Peden AA, Scheller RH (2001) A genomic perspective on membrane compartment organization. Nature **409:** 839–841

Chapman S, Faulkner C, Kaiserli E, Garcia-Mata C, Savenkov EI, Roberts AG, Oparka KJ, Christie JM (2008) The photoreversible fluorescent protein iLOV outperforms GFP as a reporter of plant virus infection. Proc Natl Acad Sci USA **105:** 20038–20043

Deniz AA, Laurence TA, Beligere GS, Dahan M, Martin AB, Chemla DS, Dawson PE, Schultz PG, Weiss S (2000) Single-molecule protein folding: diffusion fluorescence resonance energy transfer studies of the denaturation of chymotrypsin inhibitor 2. Proc Natl Acad Sci USA **97:** 5179–5184

Dreyer I, Blatt MR (2009) What makes a gate? The ins and outs of Kv-like K^+ channels in plants. Trends Plant Sci **14:** 383–390

Fasshauer D, Sutton RB, Brunger AT, Jahn R (1998) Conserved structural features of the synaptic fusion complex: SNARE proteins reclassified as Q- and R-SNAREs. Proc Natl Acad Sci USA **95:** 15781–15786

Filippini F, Rossi V, Galli T, Budillon A, D'Urso M, D'Esposito M (2001) Longins: a new evolutionary conserved VAMP family sharing a novel SNARE domain. Trends Biochem Sci **26:** 407–409

Fletcher S, Bowden SEH, Marrion NV (2003) False interaction of syntaxin 1A with a Ca^{2+}-activated K^+ channel revealed by co-immunoprecipitation and pull-down assays: implications for identification of protein-protein interactions. Neuropharmacology **44:** 817–827

Gonzalez LC Jr, Weis WI, Scheller RH (2001) A novel snare N-terminal domain revealed by the crystal structure of Sec22b. J Biol Chem **276:** 24203–24211

Grefen C, Blatt MR (2008) SNAREs: molecular governors in signalling and development. Curr Opin Plant Biol **11:** 600–609

Grefen C, Blatt MR (2012) A 2in1 cloning system enables ratiometric bimolecular fluorescence complementation (rBiFC). Biotechniques **53:** 311–314

Grefen C, Chen Z, Honsbein A, Donald N, Hills A, Blatt MR (2010) A novel motif essential for SNARE interaction with the K^+ channel KC1 and channel gating in *Arabidopsis*. Plant Cell **22:** 3076–3092

Grefen C, Honsbein A, Blatt MR (2011) Ion transport, membrane traffic and cellular volume control. Curr Opin Plant Biol **14:** 332–339

Grefen C, Karnik R, Larson E, Lefoulon C, Wang Y, Waghmare S, Zhang B, Hills A, Blatt MR (2015) A vesicle-trafficking protein commandeers Kv channel voltage sensors for voltage-dependent secretion. Nat Plants **1:** 15108

Grefen C, Lalonde S, Obrdlik P (2007) Split-ubiquitin system for identifying protein-protein interactions in membrane and full-length proteins. Curr Protoc Neurosci **Chapter 5:** Unit 5.27

Grefen C, Obrdlik P, Harter K (2009) The determination of protein-protein interactions by the mating-based split-ubiquitin system (mbSUS). Methods Mol Biol **479:** 217–233

Greitzer-Antes D, Barak-Broner N, Berlin S, Oron Y, Chikvashvili D, Lotan I (2013) Tracking Ca^{2+}-dependent and Ca^{2+}-independent conformational transitions in syntaxin 1A during exocytosis in neuroendocrine cells. J Cell Sci **126:** 2914–2923

Hecker A, Wallmeroth N, Peter S, Blatt MR, Harter K, Grefen C (2015) Binary 2in1 vectors improve in planta (co)localization and dynamic protein interaction studies. Plant Physiol **168:** 776–787

Honsbein A, Blatt MR, Grefen C (2011) A molecular framework for coupling cellular volume and osmotic solute transport control. J Exp Bot **62:** 2363–2370

Honsbein A, Sokolovski S, Grefen C, Campanoni P, Pratelli R, Paneque M, Chen Z, Johansson I, Blatt MR (2009) A tripartite SNARE-K^+ channel complex mediates in channel-dependent K^+ nutrition in *Arabidopsis*. Plant Cell **21:** 2859–2877

Hoshi T (1995) Regulation of voltage dependence of the KAT1 channel by intracellular factors. J Gen Physiol **105:** 309–328

Ishikawa-Ankerhold HC, Ankerhold R, Drummen GPC (2012) Advanced fluorescence microscopy techniques: FRAP, FLIP, FLAP, FRET and FLIM. Molecules **17:** 4047–4132

Jahn R, Scheller RH (2006) SNAREs: engines for membrane fusion. Nat Rev Mol Cell Biol **7:** 631–643

Kang G, López-Peña I, Oklejas V, Gary CS, Cao W, Kim JE (2012) Förster resonance energy transfer as a probe of membrane protein folding. Biochim Biophys Acta **1818:** 154–161

Karnik A, Karnik R, Grefen C (2013a) SDM-Assist software to design site-directed mutagenesis primers introducing "silent" restriction sites. BMC Bioinformatics **14:** 105

Karnik R, Grefen C, Bayne R, Honsbein A, Köhler T, Kioumourtzoglou D, Williams M, Bryant NJ, Blatt MR (2013b) *Arabidopsis* Sec1/Munc18 protein SEC11 is a competitive and dynamic modulator of SNARE binding and SYP121-dependent vesicle traffic. Plant Cell **25:** 1368–1382

Karnik R, Waghmare S, Zhang B, Larson E, Lefoulon C, Gonzalez W, Blatt MR (2017) Commandeering channel voltage sensors for secretion, cell turgor, and volume control. Trends Plant Sci **22:** 81–95

Karnik R, Zhang B, Waghmare S, Aderhold C, Grefen C, Blatt MR (2015) Binding of SEC11 indicates its role in SNARE recycling after vesicle fusion and identifies two pathways for vesicular traffic to the plasma membrane. Plant Cell **27:** 675–694

Kelly LA, Sternberg MJE (2009) Protein struture prediction on the web: a case study using the Phyre server. Nat Protoc **4:** 363–371

Kent HM, Evans PR, Schäfer IB, Gray SR, Sanderson CM, Luzio JP, Peden AA, Owen DJ (2012) Structural basis of the intracellular sorting of the SNARE VAMP7 by the AP3 adaptor complex. Dev Cell **22:** 979–988

Lefoulon C, Karnik R, Honsbein A, Gutla PV, Grefen C, Riedelsberger J, Poblete T, Dreyer I, Gonzalez W, Blatt MR (2014) Voltage-sensor transitions of the inward-rectifying K^+ channel KAT1 indicate a latching mechanism biased by hydration within the voltage sensor. Plant Physiol **166:** 960–975

Leyman B, Geelen D, Quintero FJ, Blatt MR (1999) A tobacco syntaxin with a role in hormonal control of guard cell ion channels. Science **283:** 537–540

Lipka V, Kwon C, Panstruga R (2007) SNARE-ware: the role of SNARE-domain proteins in plant biology. Annu Rev Cell Dev Biol **23:** 147–174

Lvov A, Chikvashvili D, Michaelevski I, Lotan I (2008) VAMP2 interacts directly with the N terminus of Kv2.1 to enhance channel inactivation. Pflugers Arch **456:** 1121–1136

Marquardt DW (1963) An algorithm for least-squares estimation of nonlinear parameters. J Soc Ind Appl Math **11:** 431–441

Murray DH, Tamm LK (2009) Clustering of syntaxin-1A in model membranes is modulated by phosphatidylinositol 4,5-bisphosphate and cholesterol. Biochemistry **48:** 4617–4625

Obrdlik P, El-Bakkoury M, Hamacher T, Cappellaro C, Vilarino C, Fleischer C, Ellerbrok H, Kamuzinzi R, Ledent V, Blaudez D, et al (2004) K^+ channel interactions detected by a genetic system optimized for systematic studies of membrane protein interactions. Proc Natl Acad Sci USA **101:** 12242–12247

Pryor PR, Jackson L, Gray SR, Edeling MA, Thompson A, Sanderson CM, Evans PR, Owen DJ, Luzio JP (2008) Molecular basis for the sorting of the SNARE VAMP7 into endocytic clathrin-coated vesicles by the Arf-GAP Hrb. Cell **134:** 817–827

Reichmann D, Rahat O, Cohen M, Neuvirth H, Schreiber G (2007) The molecular architecture of protein-protein binding sites. Curr Opin Struct Biol **17:** 67–76

Rossi V, Banfield DK, Vacca M, Dietrich LE, Ungermann C, D'Esposito M, Galli T, Filippini F (2004) Longins and their longin domains: regulated SNAREs and multifunctional SNARE regulators. Trends Biochem Sci **29:** 682–688

Sanderfoot A (2007) Increases in the number of SNARE genes parallels the rise of multicellularity among the green plants. Plant Physiol **144:** 6–17

Sieber J, Willig K, Kutzner C, Gerding-Reimers C, Harke B, Donnert G, Rammner B, Eggeling C, Hell SW, Grubmüller H, et al (2007) Anatomy and dynamics of a supramolecular membrane protein cluster. Science **317:** 1072–1076

Sottocornola B, Visconti S, Orsi S, Gazzarrini S, Giacometti S, Olivari C, Camoni L, Aducci P, Marra M, Abenavoli A, et al (2006) The potassium channel KAT1 is activated by plant and animal 14-3-3 proteins. J Biol Chem **281:** 35735–35741

Südhof TC, Rothman JE (2009) Membrane fusion: grappling with SNARE and SM proteins. Science **323:** 474–477

Sutter JU, Campanoni P, Tyrrell M, Blatt MR (2006) Selective mobility and sensitivity to SNAREs is exhibited by the *Arabidopsis* KAT1 K^+ channel at the plasma membrane. Plant Cell **18:** 935–954

Tochio H, Tsui MM, Banfield DK, Zhang M (2001) An autoinhibitory mechanism for nonsyntaxin SNARE proteins revealed by the structure of Ykt6p. Science **293:** 698–702

Tsuk S, Lvov A, Michaelevski I, Chikvashvili D, Lotan I (2008) Formation of the full SNARE complex eliminates interactions of its individual protein components with the Kv2.1 channel. Biochemistry **47:** 8342–8349

Tyrrell M, Campanoni P, Sutter JU, Pratelli R, Paneque M, Sokolovski S, Blatt MR (2007) Selective targeting of plasma membrane and tonoplast traffic by inhibitory (dominant-negative) SNARE fragments. Plant J **51:** 1099–1115

Uemura T, Ueda T, Ohniwa RL, Nakano A, Takeyasu K, Sato MH (2004) Systematic analysis of SNARE molecules in Arabidopsis: dissection of the post-Golgi network in plant cells. Cell Struct Funct **29:** 49–65

Vivona S, Liu CW, Strop P, Rossi V, Filippini F, Brunger AT (2010) The longin SNARE VAMP7/TI-VAMP adopts a closed conformation. J Biol Chem **285:** 17965–17973

Xing S, Wallmeroth N, Berendzen KW, Grefen C (2016) Techniques for the analysis of protein-protein interactions in vivo. Plant Physiol **171:** 727–758

Zhang B, Karnik R, Wang Y, Wallmeroth N, Blatt MR, Grefen C (2015) The *Arabidopsis* R-SNARE VAMP721 interacts with KAT1 and KC1 K^+ channels to moderate K^+ current at the plasma membrane. Plant Cell **27:** 1697–1717